

Near-field Decomposition of an Excited Mach 0.9 Jet - Complementary Experimental and Computational Analysis

Michael Crawley*, Rachelle L. Speth†, Datta V. Gaitonde‡, and Mo Samimy§

Mechanical and Aerospace Engineering, The Ohio State University, Columbus, OH

I. Introduction

Acoustic radiation has been a significant problem for commercial airports and aircraft carriers since the advent of turbojet engines in aeronautical applications. Commercial aviation must contend with more restrictive curfews, higher surcharges and flight path restrictions in order to appease the urban and residential areas near the airports which are perturbed by the jet noise. On aircraft carriers, the close proximity of ground crew personnel to tactical jet engines during take-off and landing creates a high potential for hearing loss. To address these issues, noise reduction concepts, most notably passive control techniques such as tabs, chevrons or lobed mixers, have been implemented in commercial vehicles, and military applications are currently being investigated. However, these modifications have a non-trivial penalty to the engine's performance, either in terms of increased weight or decreased thrust. Therefore, active control techniques are currently being investigated in order to mitigate the losses seen from passive control. In order to effectively control the production of noise, the mechanisms that produce aeroacoustic pollution must be well understood.

Lighthill¹ was the first to show that the governing equations for fluid dynamics could be rearranged into an inhomogenous wave equation. The source term, later dubbed Lighthill's stress tensor, comprises Reynolds stress, shear stress, and density fluctuations terms. Aside from the assumption of a constant sound speed, this rearrangement is exact. Therefore, complete knowledge of the source term should yield an exact solution for the acoustic far-field. In practical applications however, the full source term is unknown and certain simplifications are required. Upon the identification of coherent structures in turbulent jet shear layers,²⁻⁵ source term models based on coherent eddies have frequently been employed, to varying success. Recognizing that the acoustic far-field spectra of supersonic and subsonic jets can be represented as two distinct universal similarity spectra, independent of jet Mach number or temperature ratio, Tam *et al.*⁶ proposed a two-component source mechanism for jet mixing noise. Large-scale coherent structures (alternatively represented as instability waves) being primarily responsible for the aft angle radiation, produce spectra with a distinct amplitude peak. Fine-scale turbulence, on the other hand, produces a less coherent, more broadband acoustic field and is the dominant source of acoustic radiation at sideline angles. Experiments utilizing direct correlations between density and velocity fluctuations in the shear layers of high-speed jets and the acoustic far-field have supported this two-component source model.^{7,8}

The mechanism by which the acoustic sources produce the acoustic radiation is not well understood in the case of the subsonically-convective jet. The highly directional and highly coherent radiation produced by the large-scale structures is congruent with Mach-wave radiation, and it was initially proposed that a similar mechanism was indeed the source mechanism in both supersonic and subsonic jets.⁹ These axially extended waveforms have been identified as having wavepacket characteristics,¹⁰ which has led to the frequency-domain description of the large-scale structures. In the subsonic jet, modulation of the waveform as it is advecting through space is necessary to produce radiation to the far field. Spatial modulation of the

*Graduate Research Assistant. Student Member, AIAA

†Graduate Research Assistant. Student Member, AIAA

‡John Glenn Chair Professor and Ohio Research Scholar. Fellow, AIAA

§John B. Nordholt Professor. Fellow, AIAA

wavepacket was shown to produce the superdirective character of far-field acoustic radiation observed in subsonic jets.¹¹ Similarly, temporal modulation of the wavepacket, in terms of amplitude and envelope, has been shown to improve agreement between analytic models and the numerical results in terms of directivity and amplitude.^{12,13}

Understanding the exact spatiotemporal evolution of the large-scale structures is important to predicting and ultimately controlling their radiation production. However, in a highly turbulent jet identifying the aeroacoustic source terms is not trivial due to the dissimilar range of scales, fluctuation intensities, and structure lifetimes. In the irrotational near-field of the jet, strong evanescent waves (pseudo-sound) associated with the advection of large-scale coherent structures in the shear layer coincide with the resultant acoustic field. Therefore, in order to identify pure acoustic waves traveling to the far-field and their corresponding source events, a decomposition of the irrotational near-field into its constitutive components is required. By identification and prediction of coherence nulls between microphones in the near field, Coiffet *et al.*¹⁴ showed that the full irrotational near-field consists primarily as a linear superposition of its hydrodynamic and acoustic components. This led subsequent researchers to propose linear filters to extract the individual components from the near-field pressure, with varying degrees of success. Tinney and Jordan¹⁵ used a Fourier-based wavenumber-frequency filter method in a cold, subsonic jet to separate the the near-field pressure into supersonically- and subsonically-conveying waves (and hence, the hydrodynamic and acoustic components). The method of Kuo *et al.*¹⁶ dispensed with explicit concerns with the phase velocity of the pressure components and instead decomposed the field using Empirical Mode Decomposition and the critical frequency, as defined by Arndt *et al.*,² which demarcates the energy dominance of the acoustic and hydrodynamic components in the near-field spectra. In the work of Crawley and Samimy,¹⁷ a new decomposition method was proposed in which a spatio-temporal continuous wavelet transform is used to filter the irrotational pressure acquired experimentally in an unheated Mach 0.9 jet. They compared this new method against those of Tinney and Jordan¹⁵ and Kuo *et al.*¹⁶ and found the new method to be superior for decomposing the broadband pressure field, as well as identifying and reconstructing strongly-energetic localized bursts of energy.

Post-processing experimental and computational data using reduced order models is beneficial to looking at the jet noise mechanisms in a new way. For instance, Jordan *et al.*¹⁸ developed a method called Most Observable Decomposition (MOD) in order to better capture the modes that generate noise. They found with this technique that only 24 MOD modes were required to capture 90% of the sound energy of a Mach 0.9 turbulent jet. Of this sound energy captured, 48% is from the break up of the coherent structures after the potential core and 12% is from the convection of coherent structures. Another approach to understanding the noise sources of jets has been Proper Orthogonal Decomposition (POD) of the flow variables in the Fourier domain. This method maintains the frequency spectra and ranks modes by energy. With this method, Arndt² examined the pressure signal outside a mixing layer and found that the phase velocity was constant indicating that the jet is non-dispersive. Others have found and confirmed that the $m = 0$ mode is dominate in the low wavenumbers and contributes the most to large scale structure noise.^{19,20} Using the DNS of a Mach 0.9 jet, Freund and Colonius²¹ discovered that the modes come in pairs and resemble a wavepacket structure. This method has also been applied before to study the control of jets. Moreno *et al.*²² computed the POD of far-field microphones of no-control and microjet controlled supersonic jets and observed a 67% decrease in energy for the first mode while using microjet control. Other methods are also combined with POD (i.e. linearized stochastic estimation (LSE) and high-order stochastic estimation (HOSE)) in order to expand the available findings. Baars and Tinney²³ performed a POD based spectral High-Order Stochastic Estimation (HOSE) on experimental data simultaneously obtained in the near and far fields and determined that the hydrodynamic waveforms in the near field are linearly related to the far-field signal.

In this work, we look to combine the analysis tools of wavelet-based hydrodynamic and acoustic decomposition with that of POD in the Fourier domain in order to study a subsonic jet. The jet has been controlled with plasma actuators in order to seed the growth of large-scale structures in the jet shear layer. Concurrently, numerical simulations have been conducted using LES, which match both the jet and the actuation conditions. Through the use of various postprocessing techniques, the near-field hydrodynamic and far-field acoustic response of the jet to excitation has been analyzed over a range of structure frequencies. Preliminary work has been completed in order to decompose the irrotational near field of the jet into its constitutive hydrodynamic and acoustic components, and to begin identification of the dominant acoustic source region and acoustic emission events. The experimental and numerical databases will complement one another, as the relevant large-scale structure dynamics which lead to acoustic emission are identified, and a

simplified source model is obtained.

II. Experimental Setup

All experiments were conducted at the GDTL within the Aerospace Research Center at the Ohio State University. Compressed, dried, and filtered air is supplied to the facility from two cylindrical storage tanks with a total capacity of 43 m^3 and maximum storage pressure of 16 MPa. The air may be routed through a storage heater (not used in this study), which allows the jet to operate with a stagnation temperature up to 500°C , before expanding through a nozzle and exhausting horizontally into an anechoic chamber. Opposite the nozzle, a collector accumulates the jet and entrained air from the jet and exhausts it to the outdoors. A schematic of the anechoic chamber can be seen in Figure 1. The dimensions of the chamber are 6.20 m wide by 5.59 m long and 3.36 m tall, with internal wedge-tip to wedge-tip dimensions of 5.14 m by 4.48 m and 2.53 m, respectively. The design of the chamber produces a cutoff frequency of 160 Hz, well below the frequencies of interest. A more detailed description of the GDTL anechoic chamber properties and validation has been given by Hahn.²⁴

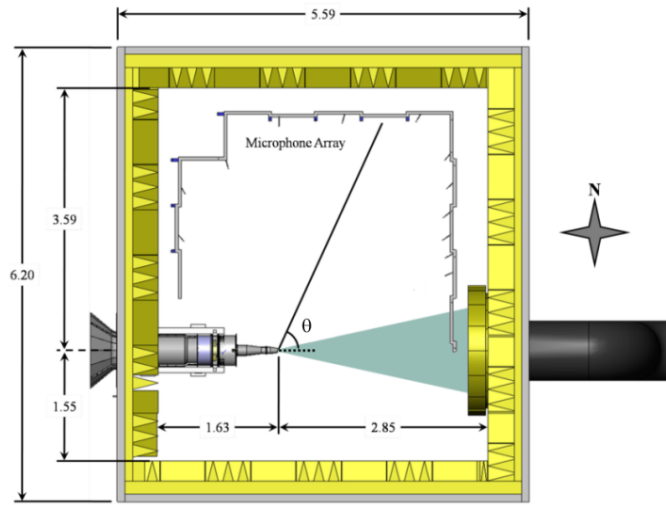


Figure 1: Plan view of the anechoic chamber at the GDTL (dimensions in meters)

For this study a converging, axisymmetric nozzle with exit diameter D of 25.4 mm (1 in.) was used. The internal contour of the nozzle was designed using a fifth order polynomial. The nozzle utilized a thick-lipped design in order to simplify the mounts for the extension, which housed the eight actuators used in this study. For the experiments reported in this paper, the jet was operated at a Mach number of 0.90, and with a total temperature ratio of unity. The Reynolds number based on the jet exit diameter was ; previous investigations using hot-wire anemometry have indicated that the initial shear layer is turbulent for this operating condition with momentum thickness 0.09 mm and boundary layer thickness 1 mm.²⁵

In the present work, the phase-averaging technique used in Sinha *et al.*²⁶ is employed in order to study the evolution of the seeded perturbations, both spatially and temporally. Points of time within this phase-averaged period (in terms of 2π) will be considered a phase (ϕ). The TTL pulse sequence, which controls the LAFPAs, is supplied to an Agilent 3320A waveform generator. The rising edge of the TTL pulse triggers a sharp drop in the output voltage of the waveform generator, which then ramps back up to the original voltage over a time interval which is shorter than the minimum forcing period. The output from the waveform generator is acquired simultaneously with the near- and far-field pressure signals using the aforementioned National Instruments hardware and software. As the forcing Strouhal number, azimuthal mode, and ramp signal are well defined, this system enables the identification of the zero phase of actuation and hence, the ability to phase-average the pressure signals over the forcing period. This ensures that the seeded perturbations can be readily identified in the noisy flow, as well as allowing pressure signals, which

were not recorded simultaneously (i.e. different near-field array positions), to be analyzed concurrently.

Analysis of the near-field response of the forced jet is not immediately straightforward due to acoustic contamination from the actuators themselves.²⁶ LAFPAs operate on a joule heating principle - the breakdown of the air between the electrodes and the ensuing flow of current results in intense heating of the air. This rapid, localized thermal perturbation produces a compression wave, which excites the shear layer. However, this compression wave is still evident as it travels through the near field. Obviously, this is an undesirable effect, as this actuator self-noise may in some cases obscure the hydrodynamic and acoustic response of the jet. In the present work, the near-field pressure signals have been preprocessed using a continuous-wavelet-based filtering algorithm, which has been specifically designed to remove the actuator self-noise while leaving the response of the jet unaltered. Further details of the filtering algorithm can be found in the references.²⁷

II.A. Localized Arc Filament Plasma Actuators

Each LAFPA consists of a pair of tungsten pin electrodes, which are placed around the nozzle perimeter 1 mm upstream of the nozzle exit. Eight uniformly spaced actuators were used in this study. The center-to-center spacing between electrode pairs for each actuator is 4 mm. The electrodes are housed in a boron nitride extension attached to the end of the nozzle. A groove with dimensions of 1 mm wide and 0.5 mm deep is machined in the boron nitride, into which the electrode tips protrude, to provide a region of low momentum flow in order to stabilize the formation of the plasma arcs. It has been shown that the existence of this groove does not substantially alter the flow field or the control authority of the LAFPAs.²⁸ A more detailed description of LAFPA characteristics can be found in Utkin *et al.*²⁹

The LAFPAs are energized by a multi-channel, high-voltage plasma power generator capable of simultaneously powering up to eight LAFPAs, which was designed and built in-house at the GDTL. In the second-generation power supply, each individual circuit consists of a switchable capacitor in line with a high voltage transformer; the arcing electrodes are connected to the secondary side of the coil. The capacitor is charged by a 100 V DC power supply when the first switch is closed and the second is opened; at the user-specified time the switches flip and it discharges through the coil. The switches are controlled by a 16-channel digital I/O card and National Instruments' Labview software, operated by a dedicated computer. The plasma generator provides independent control of the frequency, duty cycle/pulse width, and phase of each individual actuator (though not the amplitude). The pulse width was held constant at $7\mu s$, which was found to be the minimum pulse width at which the actuators consistently arced for all frequencies explored in this study.²⁸ For reference, this results in a duty cycle of 0.4% at $St_{DF} = 0.05$ and 2.0% at $St_{DF} = 0.25$. The circuit is capable of operating at up to 100 kHz, though presently it is limited to 20 kHz due to thermal concerns.

II.B. Data Acquisition

Near-field and far-field pressure measurements were acquired simultaneously, using Brüel and Kjær 1/4 inch 4939 microphones. The signal from each microphone is band-pass filtered from 20 Hz to 100 kHz using a Brüel and Kjær Nexus 2690 conditioning amplifier, and recorded using National Instruments PXI-6133 A/D boards and LabView software. The microphones are calibrated using a Brüel and Kjær 114 dB, 1 kHz sine wave generator. The frequency response of the microphones is flat up to roughly 80 kHz, with the protective grid covers removed. Voltage signals are collected at 200 kHz with 81920 data points per block; sub-blocks of 8192 data points were used when calculating short-time power spectral densities, resulting in a frequency resolution of 24.4 Hz. Ten blocks were recorded for each case resulting in four seconds of data, which has been found to be sufficient for convergence of turbulence statistics.

Far-field acoustic pressure was acquired at three polar angles: 30°, 60° and 90°, as measured from the downstream jet axis. The microphones are oriented such that the normal vector from their tips intersects the jet downstream axis at the nozzle exit. The radial distance of the microphones ranges from 101D at 30° to 145D at 60°. The near-field pressure was acquired using a linear array of sixteen microphones located along the meridional plane of the jet; the spacing varied along the array from 1D to 2D (Figure 2a). The linear array was mounted on a linear traverse system at an angle of 8.6° to the jet axis in order to match the spreading angle of the jet shear layer for this Mach number, as determined via PIV during previous studies.²⁵ The traverse was controlled using LabView and enabled the acquisition of pressure measurements at various radial positions to the jet axis. Initially, the most upstream microphone is positioned at $x/D = 1$ and $r/D = 1.20$, to ensure that the microphone tips are outside the mixing layer and do not affect the flow

field. For subsequent cases, the microphone array was incremented radially outward by $0.5D$ for a total travel distance of $7D$, for a total of 15 microphone locations in the radial direction. A schematic of the microphone locations can be found in Figure 2b.

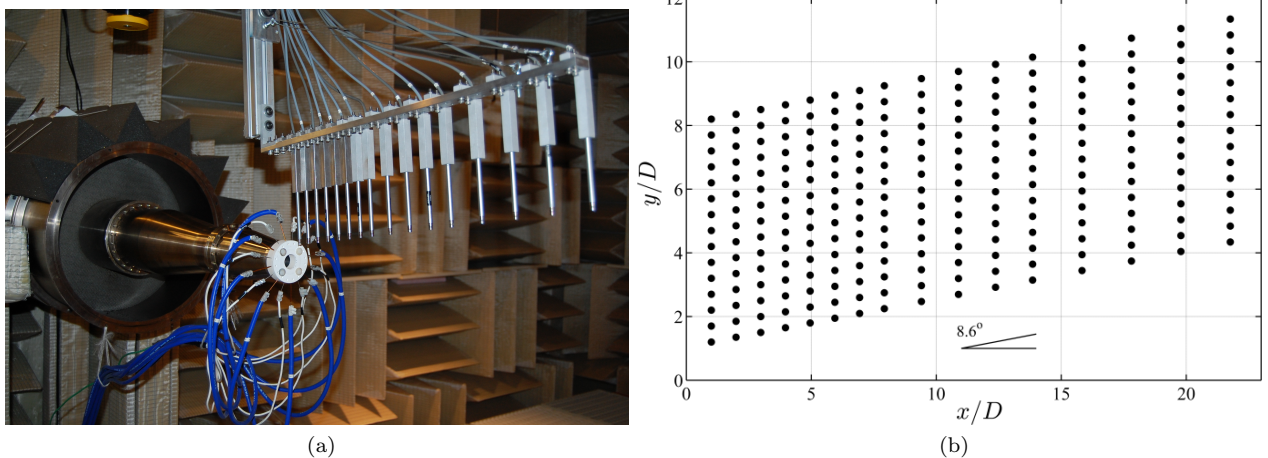


Figure 2: Photograph of anechoic chamber and nozzle, with near-field linear microphone array in foreground (a) and schematic of all near-field microphone locations (b).

III. Computational Theoretical and Numerical Model

The simulations use FDL3DI, which solves the full compressible Navier-Stokes equations, cast in strong conservative form, in curvilinear coordinates (ξ, η, ζ) . The curvilinear coordinates are obtained from a transformation from the physical space.^{30,31} The transformed non-dimensional equations in vector notation are given as:

$$\frac{\partial}{\partial \tau} \left(\frac{\vec{U}}{J} \right) + \frac{\partial \hat{F}}{\partial \xi} + \frac{\partial \hat{G}}{\partial \eta} + \frac{\partial \hat{H}}{\partial \zeta} = \frac{1}{Re} \left[\frac{\partial \hat{F}_v}{\partial \xi} + \frac{\partial \hat{G}_v}{\partial \eta} + \frac{\partial \hat{H}_v}{\partial \zeta} \right] \quad (1)$$

where $\vec{U} = \{\rho, \rho u, \rho v, \rho w, \rho E\}$ denotes the solution vector and $J = \partial(\xi, \eta, \zeta, \tau) / \partial(x, y, z, t)$ is the transformation Jacobian. Details of the various terms in Eqn. 1 may be found in Speth and Gaitonde.³² The inviscid terms are discretized with the Roe scheme,³³ combined with the MUSCL approach of van Leer.³⁴ The van Leer harmonic limiter³⁴ is used to maintain the robustness of the small scale turbulence within the simulations. The viscous terms in the governing equations are obtained with second-order centered differences and time integration is performed by a second-order diagonalized³⁵ approximately factored method³⁶ employed within a sub-iteration strategy to minimize errors due to factorization, linearization and explicit boundary condition implementation.

A 65 million point mesh is used to simulate the Mach 0.9 jet of the experiments (Fig. 3). The grid has dimensions of 685 points on the ξ direction, 455 points in the η direction, and 209 points in the ζ direction. The mesh is refined in the nozzle region then gradually stretched in the radial direction. At the exit of the nozzle, the grid maintains a constant axial spacing past the potential core length; then begins to stretch at an axial distance of $19D$. To preserve continuity, the grid has a five point overlap in the ζ direction. Characteristic boundary conditions³⁷ are applied to the upstream (outside the nozzle) and radial boundaries. Non-reflecting conditions are applied to the downstream and far field boundaries. The flow of the first ξ plane of the nozzle is specified ($\rho = 2.04 \text{ kg/m}^3$, $U = 22 \text{ m/s}$, $P = 171427 \text{ Pa}$) so that the expanded nozzle exit conditions will match the ideally expanded exit conditions of the Mach 0.9 experiments: $\rho_{jet} = 1.404 \text{ kg/m}^3$, $U_{jet} = 285.99 \text{ m/s}$, $T_{jet} = 251.31 \text{ K}$ and thus $Re = 635,308$. The nozzle geometry resembles that of the experiments including the nozzle ring on which the actuators are mounted. The velocity profile at the entrance to the nozzle is that of a uniform flow (zero at the wall and freestream everywhere else). Perturbations were not introduced into the boundary layer due to the unknown perturbations in the experiment. Therefore, the simulations have a laminar boundary layer at the nozzle exit while the experiments have a turbulent boundary layer. The previous grid study performed in Speth

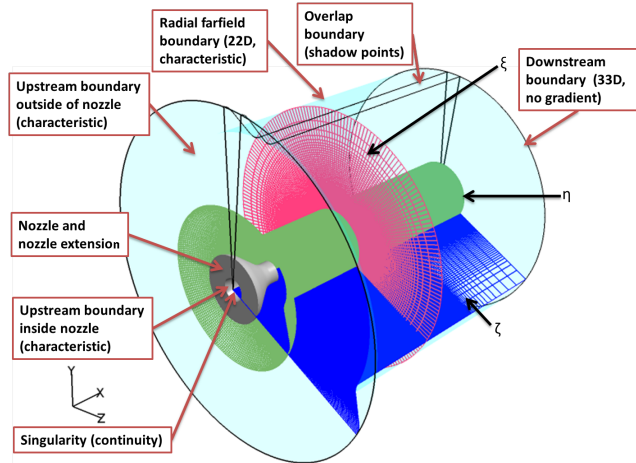


Figure 3: Computational domain

and Gaitonde³⁸ depicted that the 32 million point mesh had reasonable agreement with experiment for the mean centerline quantities. Therefore, a grid convergence study will not be performed here at this time.

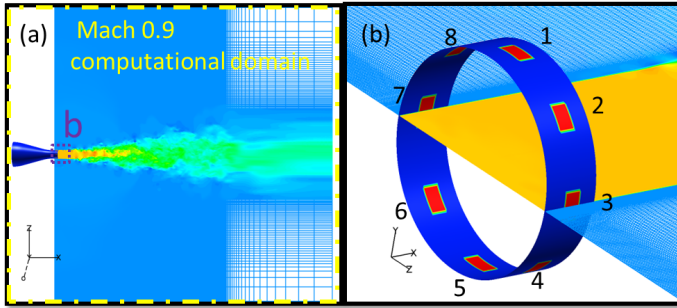


Figure 4: The computational domain including the nozzle (a), and the numerical actuator model (b)

In these simulations, the LAFPAs are modeled after the experiments using a surface heating technique to excite jet shear layer instabilities and azimuthal modes within the jet. Eight actuators are placed around the periphery of the jet on the nozzle collar at the locations and dimensions of the experiments as explained above in Section II.A. As shown in Fig. 4b, each actuator consists of a heated region of the nozzle wall which extends the azimuthal length in which the two electrodes are separated (3mm) and has an axial extent of the groove in which the electrodes are set in (1mm). The temperature of the nozzle wall was assumed to be $1.12T_{\infty}$. When the actuator is on the temperature of the actuator region increases to $5T_{\infty}$. Little difference was seen in the previous work (Speth and Gaitonde³⁹) for the temperature range measured in experiments (Utkin *et al.*⁴⁰) for a Mach number of 1.3. Unlike other acoustic drivers, the LAFPAs have a rectangular pulse, and a duty cycle which allows for a wide range of operation choices. Duty cycle is the percentage of actuator on time out of one excitation cycle. Therefore, a duty cycle of 100% results in the actuators being on all the time. A higher duty cycle (10%) was required than the one used in the experiments (1.97% for $St = 0.25$) in order to obtain control authority. The success of this simple approach has been documented in Gaitonde and Samimy,⁴¹ where, in addition to coherent structures, mean and fluctuating quantities have been compared. Furthermore, the mean flow structure with control was shown to match the theoretical predictions of Cohen and Wygnanski.⁴²

Like the experiments, the axisymmetric ($m = 0$) mode was employed to study a range of Strouhal numbers. The Strouhal numbers studied in the simulations include: 0.05, 0.15, and 0.25. Data was acquired every timestep at the point probes depicted in Fig. 2b as well as on several ξ , η , and ζ computational planes. Phase-averaged data were also computed for each of the simulations.

IV. Results

IV.A. Near-field Response to Excitation

Sinha *et al.*²⁶ previously found that each pulse from the actuators produced a perturbation, which would amplify, roll into a large-scale structure, then the structure grow, saturate, and decay as it advected through the jet shear layer. In the irrotational near-field, the signature of these large-scale structures took the form of a compact waveform, with a strong compression wave followed closely by a strong expansion wave. At low enough excitation frequencies (e.g. $St_{DF} = 0.05$), the characteristic period of this compact waveform is much less than the excitation period. Hence, the structures seeded by the excitation do not interact with one another as they evolve downstream. Because these structures evolve independently, their behavior can be thought of as representing the response of the jet to a single perturbation: the impulse response of the jet. As the excitation Strouhal number is increased, the excitation period will decrease to the point where the characteristic period of the impulse response is on the same order as, or greater than, the excitation period. As the period of actuation approaches the characteristic period of the impulse response, the waveforms extracted by the phase-averaging technique are largely unmodified from that of the impulse response; they are simply spaced closer together. As the Strouhal number is increased beyond this initial interaction Strouhal number, the phase averaged waveform resembles a sine-wave ($St_{DF} = 0.25$).

This behavior of independent evolution and periodic interactions between structures can be observed in Figure 5, which depicts the phase averaged waveforms for the experiments and computations at an axial distance of $3D$ on the first array position ($r/D = 1.5$) for different excitation frequencies. For the experimental data, the impulse response of the jet is observed at the two lowest excitation frequencies, $St_{DF} = 0.02$ and 0.05 (not shown here), as the characteristic period of the compression and expansion waves is much less than the period of excitation. For $St_{DF} = 0.15$ to 0.25 , the magnitudes of the peak and trough are nearly unchanged and the shape is largely unaffected, yet the characteristic period of the response is reduced due to the structure interactions. Further increases in the excitation Strouhal number, to $St_{DF} = 0.35$ and 0.50 , yields structures for which the amplitude has been significantly reduced, as has the characteristic period. In the case of the simulated jet, a compact response to the excitation is also observed, though with some differences with the experimental results. The amplitudes of the simulations are also greater than the experimental results. Given that the receptiveness of a shear layer to perturbations is highly sensitive to changes in shear layer characteristics and actuator locations, exact quantitative matches between the experimental and numerical database is not expected. More importantly is that the same qualitative trends are observed in both jets.

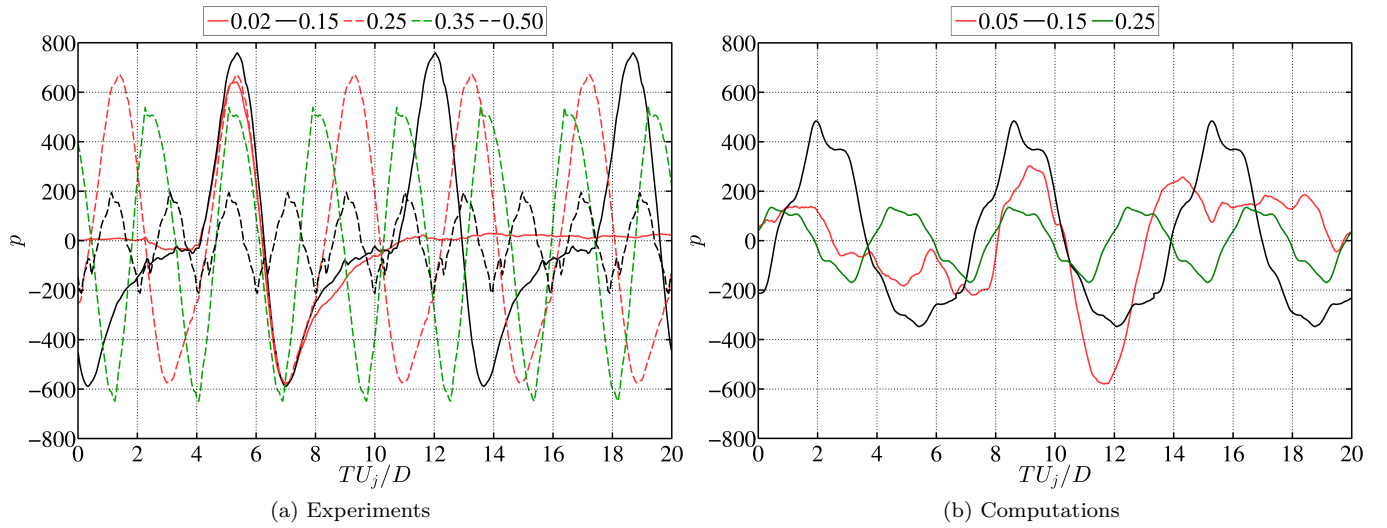


Figure 5: Phase-averaged waveforms at $x/D = 3$, $r/D = 1.5$

A simple metric for evaluating the growth, saturation, and decay of the large-scale structures generated by the excitation is the mean-square of the pressure fluctuations; these are shown in Fig. 6 along the first pressure probe array for the different excitation Strouhal cases and the baseline (0.00) no-control case.

Again, the amplitudes of the P_{ms} for the experimental and simulated jets are not identical. However, the general trends of the amplitude differences due to excitation Strouhal numbers are the same. The baseline no-control case exhibits the lowest mean square values followed by the lowest excitation Strouhal number. The mean square pressure increases with increasing excitation Strouhal number until the column mode Strouhal number is reached ($St_{DF} \approx 0.3$) at which point the mean square pressure starts to decrease with increasing excitation Strouhal number. For both experiments and simulations, increasing the excitation Strouhal number also yields an upstream shift in the saturation location. These results are consistent with those of other researchers, who have shown that perturbations of higher frequencies saturate earlier upstream than lower frequencies.^{43,44} Though some differences exist between the experimental and numerical databases, given the nature of the phenomena under study this is to be expected, and overall good agreement is found for the response of the jet to excitation.

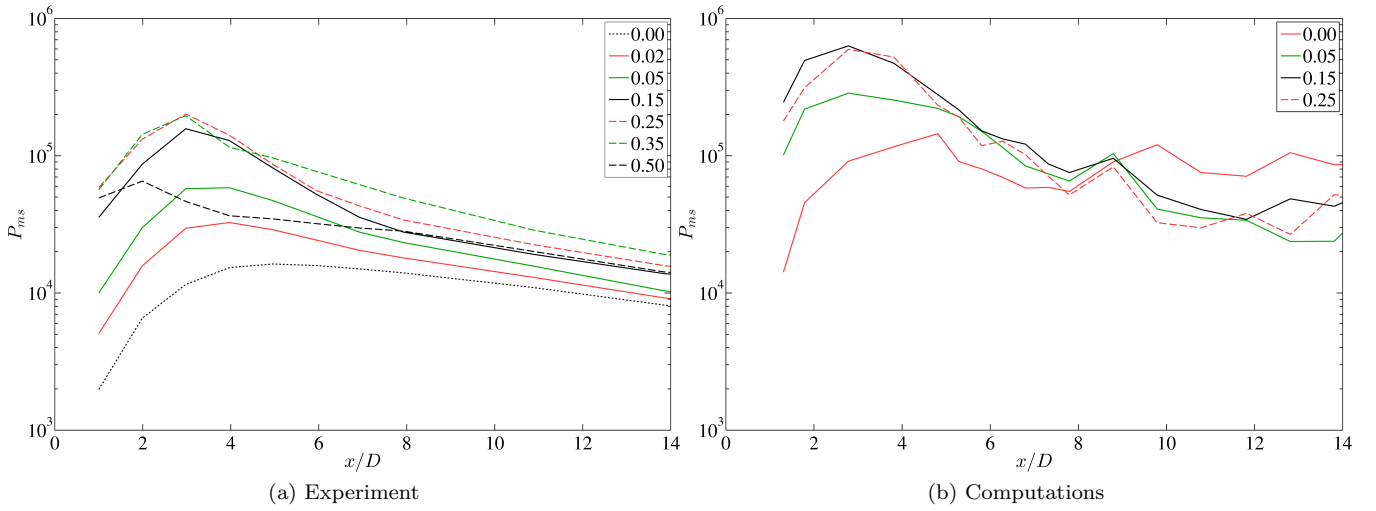


Figure 6: Mean-square pressure along the first array (first probe located at $r/D = 1.2$)

IV.B. Vortex Dynamics

Now that the validity of the simulations has been established, the large scale structures that are associated with the near-field dynamics can be studied. The phase-averaged isolevels of Q-criterion ($Q = 0.35$) colored by axial velocity with a background of dilatation in gray scale is illustrated in Fig. 7 for each excitation case. Each figure depicts two phases of the excitation period ($\phi = 0.1(2\pi)$ and $0.6(2\pi)$). In each phase, the locations of $x/D = 2$ and 4 of the first array are labeled. For the $St = 0.05$ cases (Fig. 7a), the A' and A structures are depicted in the phase $0.1(2\pi)$. At the phase of $0.6(2\pi)$, the structure in the first phase has already broken up resulting in no observable actuator induced structures in this phase for this Strouhal number.

The high frequency cases develop rollers due to the excitation that grow and interact with other actuator induced structures as they propagate downstream. This has been shown computationally by Speth and Gaitonde⁴⁵ and experimentally by Sinha *et al.*²⁶ The structures that are produced in phase $\phi = 0.6(2\pi)$ of Figs. 7b and c are the same as the impulse response structures in Fig. 7a but as the structures grow and propagate downstream they interact with the previously created actuated structure. Structures B and B' are equivalent to A and A' respectively and belong to the previous/subsequent actuator pulse. Figure 7b depicts the $St = 0.15$ case in which the structures start to interact around an axial distance of $4D$. In phase $\phi = 0.1(2\pi)$, the characteristic structures seen in Figs. 7a are seen. Half a phase later A' is broken up close to $x/D = 4$ while the ill formed B structure is colliding into the remains of A' . B' and B are similar structures to the ones denoted in the impulse case (Fig. 7a) however structure B is not as well formed as structure A . Conversely, B' is more robust than the previous A' structure. This indicates a degree of feedback response of the structures between each excitation pair.

Figure 7c depicts the isolevels of the high frequency ($St = 0.25$) case in which the structures are interacting by an axial distance of $2D$. Since, the reaction to the actuation is cyclic the structures seen at the end of

the potential core in one phase ($\phi = 0.1(2\pi)$) begin to develop in the other phase. Structure B/A' in phase $\phi = 0.1(2\pi)$ occurs when structure B collides into structure A'. This compression occurs due to the high convective velocity of B compared to A'. This interaction is quasi-linear creating a sine-like response in the near field pressure through linear superpositioning of the two actuator structures (B and A'). This quasi-linear superpositioning has been shown by Sinha *et al.*²⁶ and Crawley *et al.*⁴⁶

The structures affect the near-field as seen by the strong dilatation waves surrounding each large scale structure. In Fig. 7, the white dilatation waves correspond to an increase in pressure while the black dilatation waves correspond to a decrease in pressure. These pressure fluctuations can be readily seen in the phase-averaged pressure probes along the first array in Fig. 8a for Strouhal numbers of 0.05 and 0.25. At a phase of $\phi = 0.1(2\pi) = 36^\circ$ in Fig. 7c, the $x/D = 4$ point probe is entering a white dilatation region (increase of pressure) while the $x/D=2$ probe is entering a black dilatation wave corresponding to a decrease in pressure. In Fig. 8a, an increase of pressure is seen at $x/D = 4$ and a decrease is seen at $x/D = 2$ for the phase of 36° .

Similarly, the correlations between the points on the first array can also be related to the phase-averaged structures. Figure 8b portrays the two-point correlations of pressure comparing $x/D=4$ to $x/D=2$ on the first array for all computational Strouhal number cases. Each Strouhal number exhibits correlation peaks which are one actuation period apart. The $St=0.05$ case exhibits a large peak around $\Delta\phi = 0.15(2\pi)$ which has a pid like decay on either side until the correlation begins to grow again due to the next actuation pulse. While the $St=0.05$ case has low correlation values between actuation periods, the high frequency cases exhibit a more sine-like pattern due to the interacting structures. These correlations can be readily seen in the phase-averaged results of Fig. 7. In Fig. 7b, at $\phi = 0.1(2\pi)$, $x/D=4$ is experiencing a dark dilatation wave (decrease in pressure) and half an excitation period later ($\phi = 0.6(2\pi)$), $x/D=2$ is experiencing a dark dilatation wave also. This translates to a positive correlation in Fig. 8b at half a phase. Also for a $St=0.25$, the phase of $0.1(2\pi)$ exhibits a rising pressure region at $x/D=4$ and thereby half a phase later ($\phi = 0.6$) the $x/D=2$ location is also experiencing a rise in pressure which is indicated as a positive correlation in Fig. 8b for a $\Delta\phi = 0.5$.

To further understand the dynamics of the structures and how they relate to the near-acoustic-field spectral POD will be employed along with wavelet decomposition (discussed further in Section IV.D). First, the shear layer and near-field will be decomposed using spectral POD to validate and confirm the results from other spectral POD decompositions present in literature.^{2,18,21} Then, the wavelet decomposed data (separation of the acoustic and hydrodynamic components) of the near-field will be decomposed into the spectral modes to evaluate the relevant processes in the acoustic signal.

IV.C. Far-field Response to Excitation

The behavior of independent and periodic interaction of the jet response to excitation is not limited exclusively to the hydrodynamically-dominated regions of the jet, but in fact holds for the acoustic far-field as well, at least at angles close to the jet axis. This can be observed in Figure 9, where the phase-averaged response of the jet in the acoustic far-field at a polar angle of 30° (with respect to the downstream jet axis) has been plotted for the experimental jet. For legibility, only a select number of excitation Strouhal numbers have been included. As with the irrotational near-field, the acoustic far-field exhibits a compact waveform for the lowest excitation Strouhal numbers. For $St_{DF} = 0.15$ and 0.25 the primary expansion and compression waves remain nearly unchanged from the fundamental response aside from a slight augmentation of the peak of the compression wave. However due to the periodic excitation, the weaker expansion and compression waves are no longer identifiable, as they're subsumed by the primary waves. At higher St_{DF} , a continuous oscillation between sharp expansion and compression waves is again observed, though both the amplitude and period are reduced from the impulse response. As before, it was found that a linear superposition of the impulse response can well predict the waveform shape and amplitude at the higher excitation frequencies.

IV.D. Near-field Hydrodynamic and Acoustic Decomposition

IV.D.1. Decomposition Method

In this work, a wavelet-based decomposition method, new to the field of aeroacoustics, is utilized in order to decompose the raw near-field pressure into its hydrodynamic and acoustic components. Use of a multidimensional, continuous wavelet transform to extract intermittent events with a given spatio-temporal character is not immediately straightforward, due to the global nature of the scale factor. A speed-tuning parameter was

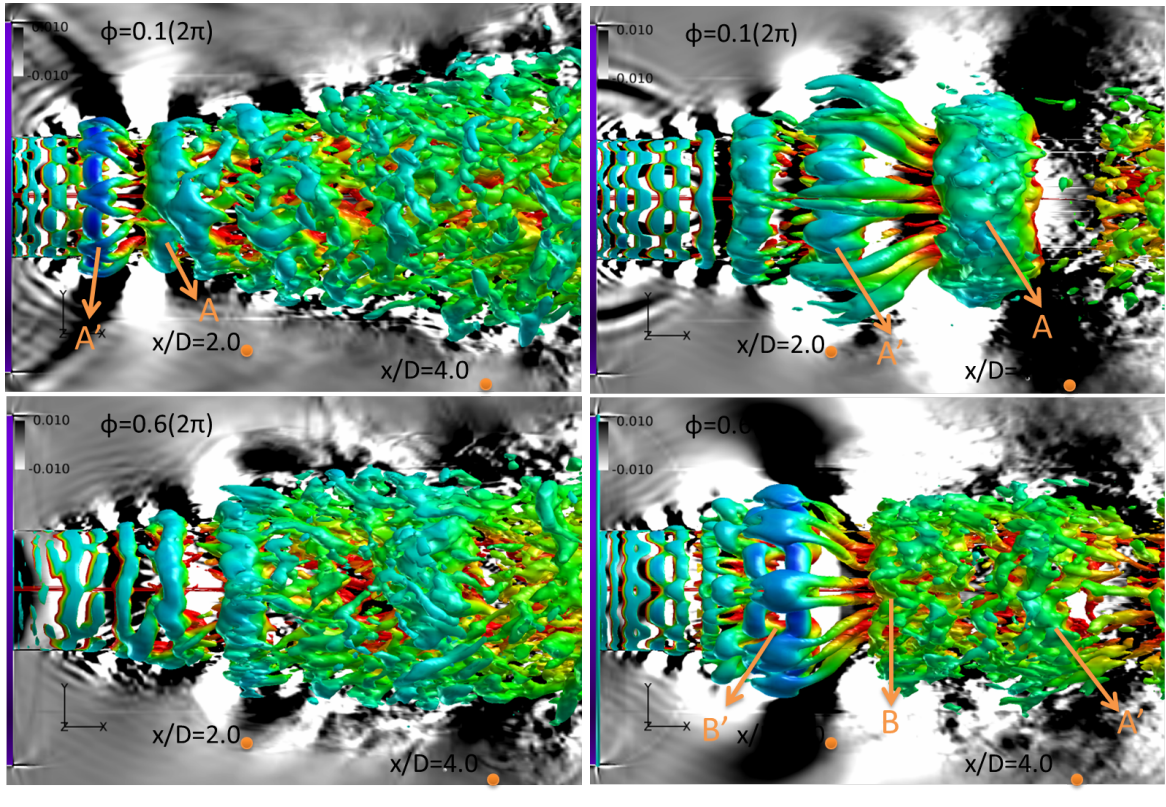
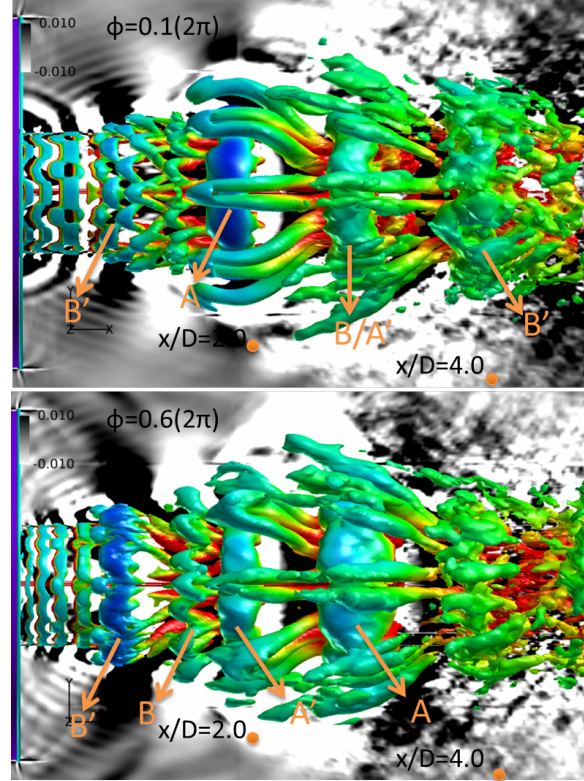
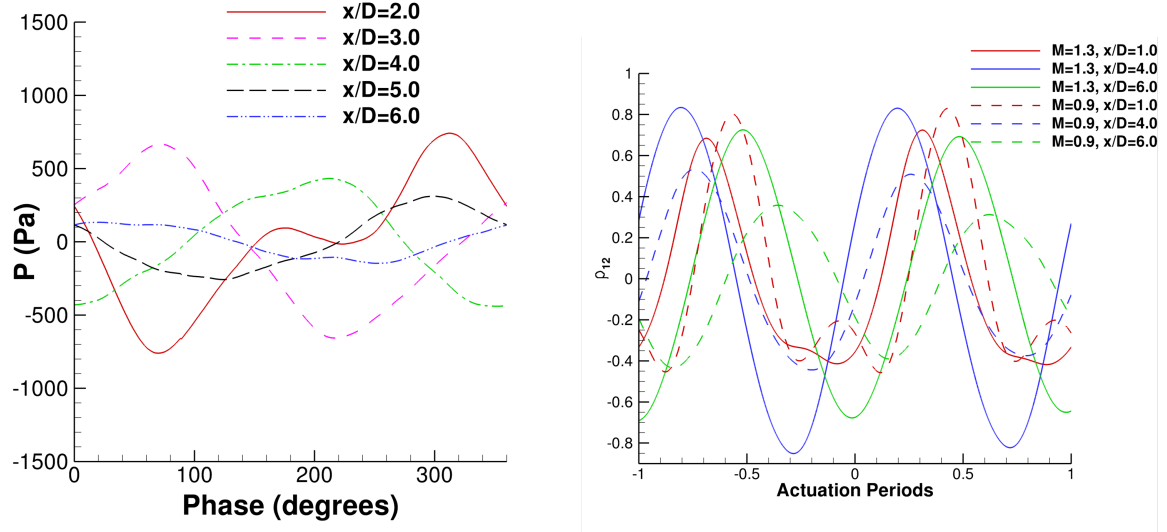
(a) $St = 0.05$ (b) $St = 0.15$ (c) $St = 0.25$

Figure 7: Simulations of the phase averaged iso-levels of Q-criterion colored by axial velocity with gray scale of dilatation



(a) Phase averaged point probes on the first array for $St=0.05$ and 0.25
(b) Two-point correlations of $x/D=2$ to $x/D=4$ for each excitation Strouhal number

Figure 8: Resultant near-field dynamics due to large scale structures

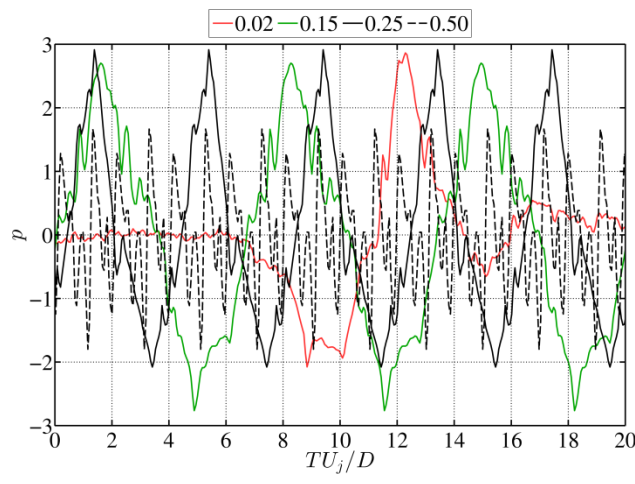


Figure 9: Phase-averaged waveforms in the acoustic far-field at 30° for select excitation frequencies, in the experimental jet.

introduced to the wavelet transform (now specifically referred to as a spatio-temporal wavelet transform) by Antoine *et al.*⁴⁷ for use in motion tracking and identification. Following the work of Kikuchi and Wang,⁴⁸ the definition for the daughter wavelets is modified to be, in two dimensions (x, t) ,

$$\psi_d(x, t; x', t', s, c) = s^{-1} \psi \left(s^{-1} c^{-1/2} (x - x'), s^{-1} c^{1/2} (t - t') \right) \quad (2)$$

From this, the spatio-temporal wavelet coefficients can be computed as

$$\tilde{p}(x', t', s, c) = \int_{-\infty}^{\infty} \int_{-\infty}^{\infty} p(x, t) \psi_d^*(x, t; x', t', s, c) dx dt \quad (3)$$

In practice however, it is usually far more computationally efficient to compute Eq. 3 in Fourier space (by the convolution theorem) and then transform the coefficients back into physical space. This leads to an alternative interpretation of the wavelet transform, that of a series of bandpass filters, the passband envelope, centroid, and width being dictated by the scale, speed, and mother wavelet.^{47, 49, 50} The decomposed signals can now be reconstructed as

$$p_h(x, t) = \frac{1}{C_\delta} \int_{0+}^{a_\infty} \frac{dc}{c} \int_{0+}^{\infty} \frac{ds}{s^2} \tilde{p}(x, t, s, c) \quad (4)$$

and

$$p_a(x, t) = \frac{1}{C_\delta} \int_{a_\infty}^{\infty} \frac{dc}{c} \int_{0+}^{\infty} \frac{ds}{s^2} \tilde{p}(x, t, s, c) \quad (5)$$

The constant factor C_δ serves as an energy scaling, and appears because we are reconstructing the signal using a different analyzing wavelet (in this case, a delta function) than the mother wavelet used in the forward transform.^{49, 50}

As with the Fourier-based decompositions, the wavelet-based decompositions are performed along each radial microphone array position, separately. Similar preprocessing of the raw signal (that is, the application of the Tukey window along the temporal dimension, zero-padding along the spatial dimension, and cubic interpolation onto a regularly spaced axial grid) was performed in order to reduce the spectral leakage inherent in the DFT (as the wavelet transform was computed in the Fourier domain). The reconstruction was then performed only over those sections of the raw signal which were not amplitude-modulated by the application of the window. In the current work, the (1+1) dimensional Morlet wavelet was chosen as the mother wavelet:

$$\psi(x, t) = e^{i(k_0 x + \omega_0 t)} e^{-(x^2 + t^2)/2} \quad (6)$$

which the reader will recognize as simply a plane wave modulated by a Gaussian. Though simplicity was a factor in this decision, previous results analyzing phase-averaged waveforms in the far-field found acoustic emissions with a characteristic waveform that share some resemblance to the Morlet wavelet.⁴⁶ The base oscillation frequencies, (k_0, ω_0) were set to $(\pm 6, 6)$ (the dual sign for k_0 being necessary to recover both forward and backward traveling waves), and $\hat{\psi}(k, 0) = 0$ and $\hat{\psi}(0, \omega) = 0$ so as to ensure that the mother wavelet met the admissibility criterion.

IV.D.2. 2D Experimental Decomposition

Before analyzing the separate fields in the context of the noise generation problem, the efficacy of the linear wavenumber-frequency filtering methodology used in this study will briefly be evaluated. Results for the decomposition of the unforced jet can be found in Figure 10, where the power spectral densities for the total, hydrodynamic, and acoustic waveforms in the unforced jet have been plotted for $x/D = 8$, $y/D = 2.2$. Three vertical lines have been overlaid on the plot, corresponding to the critical frequency, and the far-field spectral peak at 30° and 90° , respectively. The critical frequency denotes the frequency at which the near-field spectra transition from hydrodynamically-dominated to acoustically-dominated, and can be visually identified by a change in the slope of the spectral decay. This frequency has been found to scale as fy/U_c , resulting in a consistent value of unity.²⁶ The convective velocity was estimated using two-point correlations between successive microphones in the upstream region of the jet, and was found to be $0.69U_j$.

As expected, the hydrodynamic component matches well with the total signal in the low frequency portions of the spectra, while the acoustic component matches well in the high frequency portions. At both positions, the critical frequency well predicts the frequency at which the cross-over in amplitude between

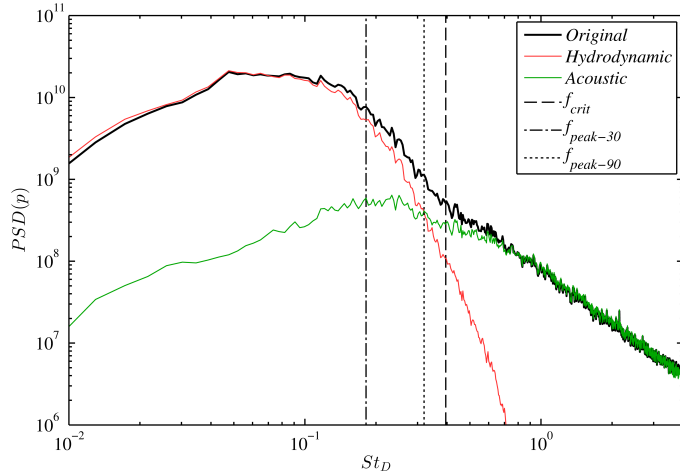


Figure 10: Spectra of the raw and decomposed fields in the unforced jet at $x/D = 8$, $y/D = 2.2$.

the hydrodynamic and acoustic components occurs. Though not shown here for brevity, A change in shape in the acoustic spectra is evident with probe position relative to the end of the potential core. At locations downstream of the end of the potential core and at low angles with respect to the jet axis, the spectrum is more peaky (reminiscent of far-field spectra at aft angles) and the acoustic spectral peak frequency matches well with the far-field peak at 30° . At locations corresponding to high angles the acoustic spectrum is more broadband and rounded (reminiscent of the well-known shape of the far-field spectra at sideline angles) and the acoustic peak frequency matches well with the far-field peak at 90° . Overall, the results found here lend strong credence to the argument that the wavelet-based filtering is producing a realistic reconstruction of the hydrodynamic and acoustic fields in both the forced and unforced jets, and accurately capturing the dynamics of the large-scale structures and their radiated noise. Currently, work is underway in order to extend the algorithm to higher-dimensions for use with the numerical database.

V. Future Work

The work to date has begun to shed light on the importance of the large-scale structure interactions in determining the acoustic far field: the structure-structure interactions (or lack thereof) appear to govern the streamwise evolution of the structures which in turn governs the acoustic emission. What remains to be done, is directly linking the relevant vortex dynamics of the large-scale structures to the acoustic emission events, and in the process identifying a simplified aeroacoustic source mechanism. To this end, the information provided separately in the experimental and numerical databases may be used to complement one another in order to provide a more complete representation of the acoustically-relevant dynamics of the large-scale structures. Additional comparisons between the experimental and simulation databases can be made in terms of vortex interactions, shortening of the potential core and spreading of the shear layer, as well as other statistics such as turbulent kinetic energy.

For the final paper, the present lines of inquire will be extended in several areas. As already mentioned, phase-locked PIV data will be obtained in the experimental jet, allowing both qualitative and quantitative measures of the large-scale structure evolutions (growth, saturation, and decay, structure-structure interactions, shear layer spreading rate, potential core length) to be evaluated from the instantaneous and phase-averaged velocity profiles with the aid of standard structure identification techniques. The addition of the decomposed LES database provides the ability to compute the full source term identified in Lighthill's acoustic analogy, as well as simplified models such as the compressible equivalents of the Lamb vector divergence and TKE Laplacian, identified by Cabana *et al.*⁵¹ as important in the sound production process in a simulated mixing layer. Finally, the structure of the radiating field can be analyzed in both the physical and wavenumber domains. Finally, spectral POD and azimuthal Fourier mode decomposition will be performed on the decomposed (acoustic and hydrodynamic) signals of the simulations in order to better understand the mechanisms that produce the acoustic waves and how these waves grow/decay, and to relate the results

of the excited jet to those of the natural jet.

Acknowledgments

Computational resources were provided by the DoD HPCMP (AFRL, NAVO and ERDC) and the Ohio Supercomputer Center. The support of this complementary experimental and computational work by the Air Force Office of Scientific Research (Dr. John Schmisseur and Dr. Rengasamy Ponnappan) is greatly appreciated. Several figures were made using Fieldview software with licenses obtained from the Intelligent Light University Partnership Program.

References

- ¹Lighthill, J., "Jet Noise," *AIAA Journal*, Vol. 1, 1963.
- ²Arndt, R. E. A., Long, D. F., and Glauser, M. N., "The proper orthogonal decomposition of pressure fluctuations surrounding a turbulent jet," Vol. 340, 1997, pp. 1–33–.
- ³Mollo-Christensen, E., "Jet Noise and Shear Flow Instability Seen From an Experimenter's Viewpoint," Vol. 34, 1967, pp. 1–7–.
- ⁴Crow, S. C. and Champagne, F. H., "Orderly structure in jet turbulence," *J. Fluid Mech.*, Vol. 48, 1971, pp. 547–591.
- ⁵Brown, G. and Roshko, A., "On Density Effects and Large Structure in Turbulent Mixing Layers," *J. Fluid Mech.*, Vol. 64, 1974, pp. 715–816.
- ⁶Tam, C. K. W., Golebiowski, M., and Seiner, J. M., "On the Two Components of Turbulent Mixing Noise from Supersonic Jets," 1996.
- ⁷Panda, J. and Seasholtz, R. G., "Experimental investigation of density fluctuations in high-speed jets and correlation with generated noise," Vol. 450, 2002, pp. 97–130–.
- ⁸Panda, J., Seasholtz, R. G., and Elam, K. A., "Investigation of noise sources in high-speed jets via correlation measurements," Vol. 537, 2005, pp. 349–385.
- ⁹Tam, C. K. W., Viswanathan, K., Ahuja, K., and Panda, J., "The Source of Jet Noise: Experimental Evidence," Vol. 615, 2008, pp. 253–292–.
- ¹⁰Jordan, P. and Colonius, T., "Wave Packets and Turbulent Jet Noise," *Annual Review Fluid Mechanics*, Vol. 45, 2013, pp. 173–95.
- ¹¹Crighton, D. G. and Huerre, P., "Shear-layer pressure fluctuations and superdirective acoustic sources," Vol. 220, 1990, pp. 355–368–.
- ¹²Sandham, N. D., Morfey, C. L., and Hu, Z. W., "Nonlinear mechanisms of sound generation in a perturbed parallel jet flow," Vol. 565, 2006, pp. 1–23–.
- ¹³Cavalieri, A. V. G., Jordan, P., Gervais, Y., Wei, M., and Freund, J. B., "Intermittent sound generation and its control in a free-shear flow," Vol. 22, 2010, pp. 115113–.
- ¹⁴Coiffet, F., Jordan, P., Delville, J., Gervais, Y., and Ricaud, F., "Coherent structures in subsonic jets: a quasi-irrotational source mechanism?" Vol. 5, No. 1, 2006, pp. 67 – 89–.
- ¹⁵Tinney, C. E. and Jordan, P., "The near pressure field of co-axial subsonic jets," Vol. 611, 2008, pp. 175–204–.
- ¹⁶Kuo, C.-W., Buisson, Q., McLaughlin, D. K., and Morris, P. J., "Experimental Investigation of Near-Field Pressure Fluctuations Generated by Supersonic Jets," 2013.
- ¹⁷Crawley, M. and Samimy, M., "Decomposition of the Near-field Pressure in a Forced Subsonic Jet," *20th AIAA/CEAS Aeroacoustics Conference*, June 2014.
- ¹⁸Jordan, P., Schlegel, M., Stalnov, O., Noack, B. R., and Tinney, C. E., "Identifying noisy and quiet modes in a jet," *13th AIAA/CEAS Aeroacoustics Conference (28th AIAA Aeroacoustics Conference)*, 2007.
- ¹⁹Hall, J. W., Pinier, J. T., Hall, A. M., and Glauser, M. N., "A Spatio-Temporal Decomposition of the Acoustic Source in a Mach 0.85 Jet," *45th AIAA Aerospace Sciences Meeting and Exhibit*, 2007.
- ²⁰Tinney, C. E., Jordan, P., Hall, A. M., Delville, J., and Glauser, M., "A time resolved estimate of the turbulence and sound source mechanisms in a subsonic jet flow," *Journal of Turbulence*, Vol. 8, No. 7, 2007, pp. 1–20.
- ²¹Freund, J. and Colonius, T., "POD Analysis of Sound Generation by a Turbulent Jet," *40th AIAA Aerospace Sciences Meeting and Exhibit*, 2002.
- ²²Moreno, D., Krothapalli, A., and Greska, B., "The use of Proper Orthogonal Decomposition Method in the Study of High Speed Jet Noise," *9th AIAA/CEAS Aeroacoustics Conference and Exhibit*, 2003.
- ²³Baars, W. J. and Tinney, C. E., "POD based spectral Higher-Order Stochastic Estimation," *48th AIAA Aerospace Sciences Meeting Including the New Horizons Forum and Aerospace Exposition*, 2010.
- ²⁴Hahn, C., *Design and Validation of the New Jet Facility and Anechoic Chamber*, Ph.D. thesis, The Ohio State University, Columbus, OH, 2011.
- ²⁵Kearney-Fischer, M., Kim, J.-H., and Samimy, M., "Control of a High Reynolds Number Mach 0.9 Heated Jet Using Plasma Actuators," *Physics of Fluids*, Vol. 21, No. 9, 2009.
- ²⁶Sinha, A., Alkandry, H., Kearney-Fischer, M., Samimy, M., and Colonius, T., "The Impulse Response of a High-Speed Jet Forced with Localized Arc Filament Plasma Actuators," *Physics of Fluids*, 2013.
- ²⁷Alkandry, H., Crawley, M., Sinha, A., Kearney-Fischer, M., and Samimy, M., "An Investigation of the Irrotational Near Field of an Excited High-Speed Jet," *51st AIAA Aerospace Sciences Meeting*, 2013.

- ²⁸Hahn, C., Kearney-Fischer, M., and Samimy, M., "On factors influencing arc filament plasma actuator performance in control of high speed jets," *Experiments in Fluids*, Vol. 51, No. 6, 2011, pp. 1591–1603.
- ²⁹Utkin, Y., Keshav, S., Kim, J.-H., Kastner, J., Adamovich, I., and Samimy, M., "Characterization of Localized Arc Filament Plasma Actuators Used for High-speed Flow Control," *AIAA Paper 2007-0787*, 2007.
- ³⁰Vinokur, M., "Conservation Equations of Gasdynamics in Curvilinear Coordinate Systems," *J. Comp. Phys.*, Vol. 14, 1974, pp. 105–125.
- ³¹Steger, J., "Implicit Finite-Difference Simulation of Flow about Arbitrary Two-Dimensional Geometries," *AIAA Journal*, Vol. 16, No. 7, July 1978, pp. 679–686.
- ³²Speth, R. and Gaitonde, D., "The Effect of Laminar Nozzle Exit Boundary Layer Thickness on a Mach 1.3 Jet With and Without Control," *42nd AIAA Fluid Dynamics Conference and Exhibit*, 2012.
- ³³Roe, P., "Approximate Riemann Solvers, Parameter Vectors and Difference Schemes," *Journal of Computational Physics*, Vol. 43, 1981, pp. 357–372.
- ³⁴van Leer, B., "Towards the Ultimate Conservation Difference Scheme V, A Second-Order Sequel to Godunov's Method," *Journal of Computational Physics*, Vol. 32, 1979, pp. 101–136.
- ³⁵Pulliam, T. and Chaussee, D., "A Diagonal Form of an Implicit Approximate-Factorization Algorithm," *J. Comp. Phys.*, Vol. 39, No. 2, 1981, pp. 347–363.
- ³⁶Beam, R. and Warming, R., "An Implicit Factored Scheme for the Compressible Navier-Stokes Equations," *AIAA Journal*, Vol. 16, No. 4, 1978, pp. 393–402.
- ³⁷Bellan, J., "Supercritical (and Subcritical) Fluid Behavior and Modeling: Drops, Streams, Shear and Mixing Layers, Jets and Sprays," *Prog. Energy Combust. Sci.*, Vol. 26, 2000, pp. 329–366.
- ³⁸Speth, R. and Gaitonde, D., "Correlation of Near Field Pressure with Coherent Structures in an Excited Mach 1.3 Jet," *ASME 2013 Fluids Engineering Division Summer Meeting*, , No. FEDSM2013-16495, 2013.
- ³⁹Speth, R. and Gaitonde, D., "Parametric Study of a Supersonic Jet Subjected to Plasma-based Flapping Mode Excitation," *AIAA Paper 2012-0901*, 2012.
- ⁴⁰Utkin, Y., Keshav, S., Kim, J.-H., Kastner, J., Adamovich, I., and Samimy, M., "Use of Localized Arc Filament Plasma Actuators for High Speed Jet Control," *J. Phys. D: Applied Physics*, Vol. 40, Feb 2007, pp. 685–694.
- ⁴¹Gaitonde, D. and Samimy, M., "Coherent structures in plasma-actuator controlled supersonic jets: Axisymmetric and mixed azimuthal modes," *Phys. Fluids*, Vol. 23, No. 9, 2011.
- ⁴²Cohen, J. and Wygnanski, I., "The evolution of instabilities in the axisymmetric jet. Part 2. The flow resulting from the interaction between two waves," *J. Fluid Mech.*, Vol. 176, 1987, pp. 221–235.
- ⁴³Suzuki, T. and Colonius, T., "Instability waves in a subsonic round jet detected using a near-field phased microphone array," *Journal of Fluid Mechanics*, Vol. 565, 2006, pp. 197–226.
- ⁴⁴Ukeiley, L. S. and Ponton, M. K., "On the near field pressure of a transonic jet," *International Journal of Aeroacoustics*, Vol. 3, No. 1, 2004, pp. 43–66.
- ⁴⁵Speth, R. and Gaitonde, D., "Near Field Pressure and Associated Coherent Structures of Excited Jets," *4th Joint US-European Fluids Engineering Summer Meeting*, , No. FEDSM2014-21186, 2014.
- ⁴⁶Crawley, M., Sinha, A., and Samimy, M., "Near-field Pressure and Far-field Acoustic Response of Forced High-Speed Jets," *52nd Aerospace Sciences Meeting*, 2014.
- ⁴⁷Antoine, J.-P., Murenzi, R., Vandergheynst, P., and Ali, S. T., *Two-Dimensional Wavelets and their Relatives*, Cambridge University Press, 2004.
- ⁴⁸Kikuchi, K. and Wang, B., "Spatiotemporal Wavelet Transform and the Multiscale Behavior of the Madden-Julian Oscillation," Vol. 23, 2010, pp. 3814–3834–.
- ⁴⁹Torrence, C. and Compo, G. P., "A Practical Guide to Wavelet Analysis," Vol. 79, No. 1, 1998, pp. 61–78–.
- ⁵⁰Farge, M., "Wavelet Transforms and Their Applications to Turbulence," Vol. 24, 1992, pp. 395–457–.
- ⁵¹Cabana, M., Fortuné, V., and Jordan, P., "Identifying the radiating core of Lighthill's source term," *Theoretical Computational Fluid Dynamics*, Vol. 22, 2008, pp. 87–106.